Probing AGN-ISM Feedback through Extended X-ray Emission in ESO 137-G034

D. L. Król , G. Fabbiano, M. Elvis , A. Trindade Falcão, A. Middei, A. Middei

¹ Center for Astrophysics | Harvard & Smithsonian, 60 Garden Street, Cambridge, MA 02138, USA
 ² NASA-Goddard Space Flight Center, Code 662, Greenbelt, MD 20771, USA
 ³ INAF Osservatorio Astronomico di Roma, 10 Via Frascati 33, 00078 Monte Porzio Catone, RM, Italy
 ⁴ Space Science Data Center, 12 Agenzia Spaziale Italiana, Via del Politecnico snc, 00133 Roma, Italy
 ⁵ School of Mathematics, Statistics and Physics, Newcastle University, Newcastle upon Tyne NE1 7RU, UK
 ⁶ Max Planck Institute for Extraterrestrial Physics, Giessenbachstrasse, 85741 Garching bei München, Germany

ABSTRACT

We present a detailed analysis of the X-ray emission of the Compton-thick (CT) AGN ESO 137-G034 based on deep ($\sim 230 \,\mathrm{ks}$) Chandra observations. As in other CT AGNs, the morphology of the emission is elongated, approximately following the [O III] ionization bicone. With spatially resolved spectral modeling, we show that the extended emission within the bi-cone regions is most readily explained as from a mixture of photo-ionized gas and shock-heated plasma, reflecting the combined effects of radiative and kinematic AGN feedback. By comparing the morphology of the X-ray emission in narrow spectral bands and that of the 3 cm radio jet, we find suggestive evidence of thermal, possibly shocked emission associated with the SE termination of the radio jet. This interpretation is also supported by the lack of [O III] relative to the 0.3 - 3.0 keV flux in the inner 3" (~ 600 pc) of the SE cone, which would be consistent with an additional thermal X-ray component on top of the photonized emission of an outflowing wind. A similar effect is only seen within the inner 1" (200 pc) of the NW cone. In the radial profile of the [OIII]/X-ray flux ratio and the X-ray hardness ratio within the inner $\sim 3''$ $(\sim 600 \,\mathrm{pc})$ of the SE cone we see an asymmetry, with no counterpart in the NW cone. We detect soft extended X-ray emission in the cross-cones which may originate from the interaction of an embedded radio jet with a clumpy interstellar medium (ISM). These results highlight the importance of both radiative and mechanical feedback in shaping the circumnuclear environment of ESO 137-G034.

Keywords: High energy astrophysics (739), Active galactic nuclei (16), X-ray active galactic nuclei (2035), Diffuse radiation (383), Interstellar medium (847), Shocks (2086), AGN host galaxies (2017)

1. INTRODUCTION

The disagreement between galaxies' observed luminosity function and the mass function predicted by the ΛCDM simulations of the large scale structures is a long-standing problem, since the observed distribution deviates from the shape predicted by simulations, especially for the lowest and highest galactic masses (Benson et al. 2003; Schechter 1976). The observed lower number of low-mass galaxies can be tied to the impact of supernovae on the interstellar medium (ISM) (Kereš et al. 2009), but to explain the deficit of the highest luminosity galaxies, a much more powerful mechanism is required. Since most massive galaxies are believed to harbor a supermassive black hole (SMBH), active galactic nuclei (AGN) are a compelling source of the required energy

(Fabian 2012). Strong coupling of AGN and galaxy evolution is also supported by a tight correlation between the SMBH and host galaxy properties (e.g., $M-\sigma$ relation Kormendy & Ho 2013), making the understanding of AGN-ISM interactions, known as AGN feedback, an important piece of understanding galaxy evolution. This picture becomes more complex as new results obtained by JWST suggest that the SMBH-to-galaxy mass ratios at high redshifts are extremely high, indicating either very rapid initial BH growth and/or a heavy seed origin (see, e.g., Adamo et al. 2024; Bogdán et al. 2024; Maiolino et al. 2024).

While population studies can provide insights into the role of AGN in galaxy evolution, high-resolution observations of AGN offer the unique opportunity to observe

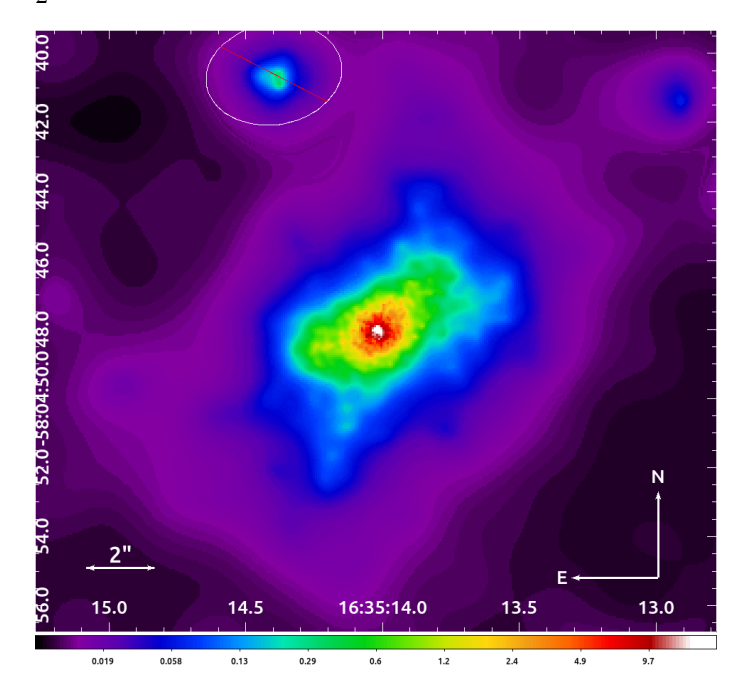


Figure 1. Chandra ACIS-S3 (CCD ID=7) image of ESO 137-G034, merged from observations listed in Tab. 1. The image has been binned with 1/8 pixel size and adaptively smoothed. Crossed circle marks the point source excluded from the analysis.

feedback as it occurs, allowing to probe different feedback avenues. In particular, high-resolution X-ray observations of the extended emission around Compton Thick (CT) AGN can shed light on the complex nature of AGN-ISM interactions, as X-rays are particularly effective in tracing the mechanisms behind this coupling, including ISM photoionization, jet-ISM shocks, and large-scale winds. Thanks to the CT nature of these sources, the central continuum exhibits a lower apparent flux, enabling detailed analysis of the diffuse emission (see recent review by Fabbiano & Elvis 2022).

The diffuse X-ray emission of Compton-Thick (CT) AGN tends to roughly trace the bi-cone morphology of regions characterized by high $[OIII]/H\alpha$ ratios in optical data (Schmitt et al. 2003; Fischer et al. 2013). These ionization cones are believed to be excited by AGN nuclear radiation "collimated" by the torus in the standard AGN model (Wilson et al. 1996). X-ray data with sufficient spatial and spectral resolution add much more to the story. Spatially resolved X-ray spectroscopy reveals that the emission from cone regions cannot be characterized purely by photoionized plasma emission, and requires an additional thermal plasma component (e.g., Fabbiano et al. 2018; Wang et al. 2011a; Travascio et al. 2021; Trindade Falcao et al. 2023). Shock-heated thermal plasma can be traced by an excess of the emission at $\sim 1 \, \mathrm{keV}$, an energy band containing the Ne IX and Ne X

lines, as well as a contribution from the broader Fe-L complex (see Wang et al. 2011a; Paggi et al. 2012), which serves as a tracer of this thermal component. Moreover, diffuse X-ray emission extends in both the bi-cone and cross-cone directions (Fabbiano et al. 2018; Ma et al. 2020), hinting at either a "leaky", porous torus geometry (Fabbiano et al. 2018) or interaction of a radio jet with a patchy, dense ISM (Fabbiano et al. 2022).

In this paper, we analyze deep Chandra ($\sim 235\,\mathrm{ks}$) observations of ESO 137-G034, with the goal of disentangling different emission mechanisms, and corresponding feedback modes, in the cone and cross-cone regions. ESO 137-G034 is an S0/a galaxy hosting a Seyfert type II AGN (Ferruit et al. 2000) at z=0.009 ($D_L=41.21\,\mathrm{Mpc}$; 1" $\simeq 200\mathrm{pc}$ Koss et al. 2022). ESO 137-G034 was part of a program targeting AGN in search of extended hard X-ray emission (Ma et al. 2020), showing a clear extent in 50 ks Chandra observations.

In Sec. 2, we describe the observations, astrometric alignment, and data reduction. In Sec. 3, we analyze the morphology of the extended emission through azimuthal and radial profile extractions across different energy bands and regions. In Sec. 4, we model the spectra of the various source regions. In Sec. 5, we interpret our results and discuss the origin of the emission in different parts of the source. In Sec. 6, we summarize our findings.

In all calculations we assumed flat ΛCDM cosmology with $H_0 = 69.3\,\mathrm{km\,s^{-1}\,Mpc^{-1}}$ and $\Omega_m = 0.287$ (Hinshaw et al. 2013). Though the paper we refer to the soft energy range as $0.3-1.5\,\mathrm{keV}$, medium as $1.5-4.0\,\mathrm{keV}$ and hard as $4.0-7.0\,\mathrm{keV}$. All position angles are measured from west to north.

2. DATA REDUCTION

ESO 137-G034 was observed 11 times (see exposures details in Tab.1) by *Chandra*'s (Weisskopf et al. 2002) Advanced CCD Imaging Spectrometer (ACIS) (Garmire et al. 2003). We combined all available data and followed standard *Chandra* data reduction procedures using CIAO v4.16 (Fruscione et al. 2006) with CALDB v4.11.5, starting with the chandra_repro¹ reprocessing script. To ensure that astrometry corrections are calculated with respect to position of the nucleus, we followed the approach by Fabbiano et al. (2017). Offsets were calculated based on the position of a centroid around the maximum counts pixel in the 5-7 keV energy range for each obsID. We chose the longest obser-

¹ Description of all CIAO scripts can be found at https://cxc.cfa.harvard.edu/ciao/ahelp/index_alphabet.html

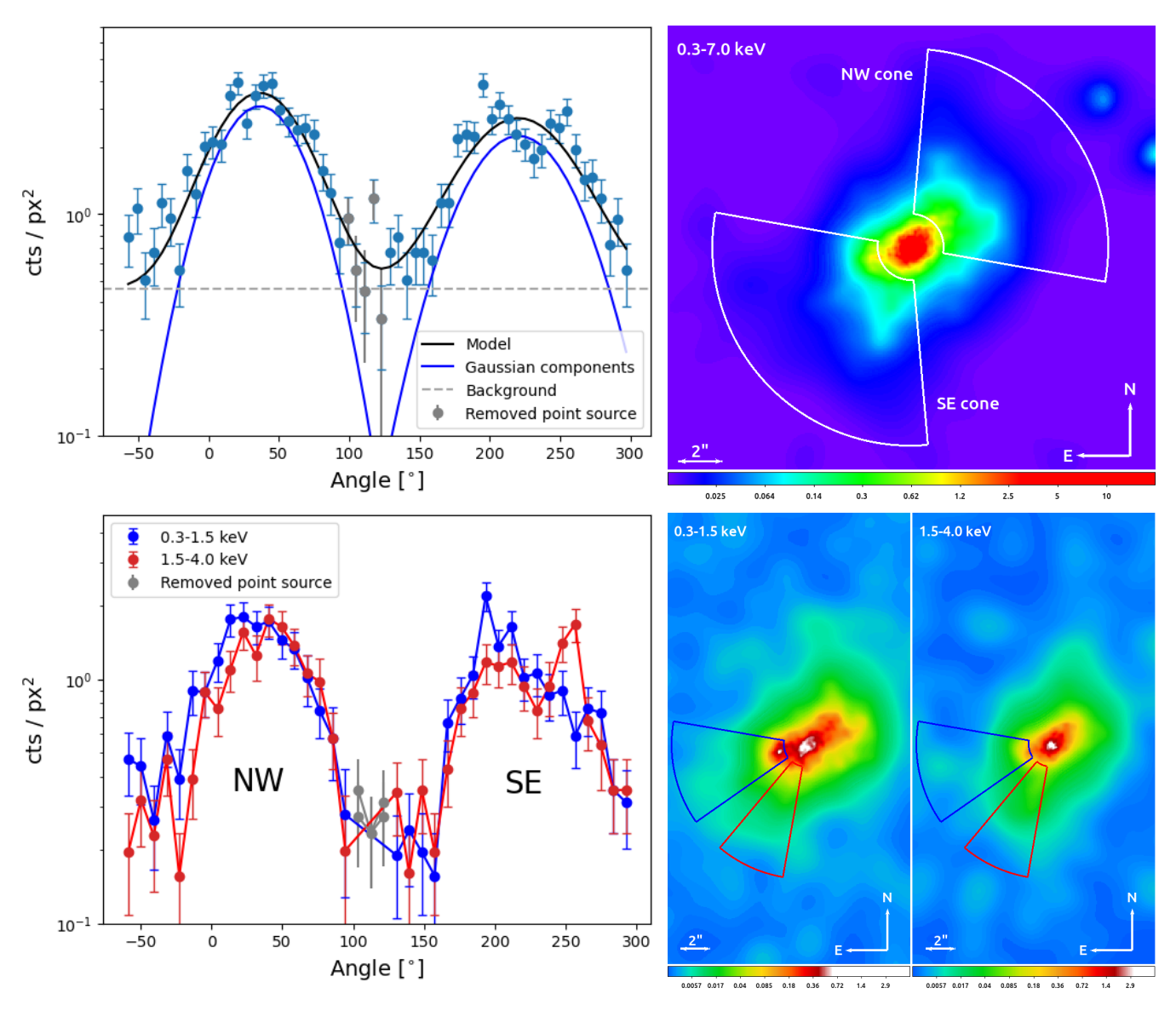


Figure 2. Left panels: Azimuthal profiles of the extended emission extracted between 1.5" and 9" from the nucleus, based on the merged *Chandra* data image. The upper left panel shows the profile for the 0.3–7.0 keV energy range, overlaid with the best-fit model (dark gray line), which consists of two Gaussian components (dark blue) and a constant background (dashed gray). Gray points indicate directions where point sources were removed. The lower left panel shows azimuthal profiles for two energy ranges: 0.3–1.5 keV (blue line) and 1.5–4.0 keV (red line). Position angles are measured from the West to the North on the sky. Right panels: The upper right panel displays the adaptively smoothed, merged image in the 0.3–7.0 keV range, overlaid with the azimuthal profile extraction region. Directions of peak emission in the 0.3–1.5 keV and 1.5–4.0 keV bands are marked in blue and red, respectively. The lower right panel shows the adaptively smoothed emission in the 0.3–1.5 keV and 1.5–4.0 keV respectively.

vation (21422) as the reference. Analysis was carried out on images binned with 1/8 of ACIS native pixel size and then smoothed with 2 pixel Gaussians. The derived offsets are listed in Tab. 1. The resulting adaptively smoothed merged image in the $0.3-7.0\,\mathrm{keV}$ band is shown in Fig. 1. The X-ray source is clearly extended to the NW and SE on scales of $\sim 10''$ (2 kpc) from the nucleus, in what may be a bicone structure as seen in many other CT AGNs (Fabbiano & Elvis 2022). Since

we are interested in the properties of any extended emission, to identify point sources so that they could be excluded from the analysis, we employed the wavdetect algorithm with the scales parameter set to: 1 px, 2 px, 4 px, 8 px, and 16 px. Other parameters of the script were set to their default values. Only one point source was detected within 9" of the nucleus. We removed it and replaced it with pixel values interpolated from the data at the same distance from the nucleus using the

Table 1. Details on Analyzed Data, including the ObsID number, date of the observation, exposure time and astrometry offset (Δx and Δy), see Sec. 2 for the details.

ObsID	Date	Exposure Time	Δx	Δy
		[ks]	pixels	pixels
21422	2020-10-18	44.76	reference	
25268	2023-03-29	10.13	-1.95	-1.53
25842	2023-10-28	9.64	-0.85	-0.52
25843	2023-03-10	29.15	-1.51	-0.78
25844	2022-01-12	22.41	-1.17	-2.09
25845	2023-06-28	28.50	1.34	-0.92
25846	2022-01-14	10.52	0.43	-1.59
27770	2023-03-30	34.05	-1.70	-0.30
28912	2023-09-15	26.39	-0.17	-1.17
28995	2023-10-28	9.66	0.55	-0.39
28996	2023-10-29	8.99	0.70	0.38

Note—Data set DOI: https://doi.org/10.25574/cdc.374

Table 2. Background Subtracted Excess Data Counts over the Model PSF for 1.5'' - 8'' Conical Regions

Energy	Cone NW	Cone SE	Cross-cone SW	Cross-cone NE
keV	$\mathrm{cts/px}^2$	$\mathrm{cts/px}^2$	$\mathrm{cts/px}^2$	$\mathrm{cts/px}^2$
0.5 - 7.0	683 ± 28	647 ± 28	134 ± 15	118 ± 15
0.5 - 1.5	333 ± 19	314 ± 18	82 ± 10	57 ± 8
1.5 - 3.0	256 ± 17	230 ± 16	39 ± 8	34 ± 8
3.0 - 4.0	40 ± 8	44 ± 8	4 ± 4	4 ± 4
4.0 - 5.0	14 ± 6	20 ± 6	-1 ± 4	7 ± 5
5.0 - 6.0	5 ± 5	9 ± 5	3 ± 4	-3 ± 4
6.0 - 7.0	23 ± 8	15 ± 7	-2 ± 5	5 ± 6

dmfilth procedure. The area corresponding to the removed point was excluded from spectral analysis and is marked in gray in all radial and azimuthal profiles.

3. MORPHOLOGY OF X-RAY EXTENDED EMISSION

3.1. Azimuthal profiles

To determine the core and cross-cone extraction regions, we examined the azimuthal profile of the extended emission. In particular, we extracted profiles binned in 6° intervals within an annulus spanning 1.5" to 9" from the nucleus (see top-left panel of Fig. 2). The profile was

fitted with a combination of two Gaussians of the form $A_i \exp\left[-\frac{(\phi-\phi_i)^2}{2\sigma_i^2}\right]$ plus a constant background. The best-fit parameters are: $\phi_1=(35\pm 3)^\circ$, $\phi_2=(219\pm 3)^\circ$, $\sigma_1=(38\pm 4)^\circ$, $\sigma_2=(30\pm 3)^\circ$, $A_1=(2.7\pm 0.2)\,\mathrm{cts/px^2}$, and $A_2=(3.6\pm 0.3)\,\mathrm{cts/px^2}$. Based on that we estimate the bicone region to be comprised between $-10^\circ-85^\circ$ (NW) and $170^\circ-275^\circ$ (SE). We define cross-cone the complementary regions. These regions are indicated in the top right panel of Fig. 2.

While the overall X-ray extended emission morphology follows the bi-cone/cross-cone structure, but the azimuthal profile of the south-east (SE) cone shows two distinct maxima at $\sim 195^\circ$ and $\sim 255^\circ$ as indicated in the bottom-left panel of Fig. 2. These peaks are pronounced in different energy bands: $\sim 195^\circ$ maxima more at the soft (0.3–1.5 keV) energy band, while the $\sim 255^\circ$ peak appears in medium (1.5–4.0 keV) energy band (see the profiles and images in the bottom panels of Fig. 2)

3.2. Radial profiles

3.2.1. PSF simulations

To assess the significance of the extended emission in different energy ranges, we performed simulations of the *Chandra* point spread function (PSF). First, for each obsID, we extracted the nuclear spectra from a circular region of radius 1.5" using the specextract routine and fitted phenomenological models to describe the spectral shape.

Next, we simulated the *Chandra* PSF using ChaRT (Carter et al. 2003) and MARX (Davis et al. 2012), with the fitted spectral model as input. For each pointing, we performed 50 PSF simulations using ChaRT, and derived the mean PSF, while the differences in the PSF realizations were adopted as errors. Each resulting ray file was then converted to a pseudo-event file with MARX, assuming an ASPECT blur of 0.07 (see Appendix 5 in Ma et al. 2023). Increasing the ASPECT blur to 0.20 does not significantly change the results. All simulations were then combined into a single pseudo-event file using the dmmerge procedure. Finally, we normalized the PSF to match the counts number in inner 1.5" of the source in each energy band.

3.2.2. Radial Emission Profiles

The cone and cross-cone regions are overlaid on the emission maps in different energy bands in Fig. 3. Using the merged data with 1/8 px binning, we extracted radial surface brightness profiles for each region in six energy bands: $0.5{\text -}1.5\,\mathrm{keV},\,1.5{\text -}3.0\,\mathrm{keV},\,3.0{\text -}4.0\,\mathrm{keV},\,4.0{\text -}5.0\,\mathrm{keV},\,5.0{\text -}6.0\,\mathrm{keV},\,$ and $6.0{\text -}7.0\,\mathrm{keV}.$ The minimum radial bin size was set to 0.246'' and adjusted to ensure at least 10 counts per bin.

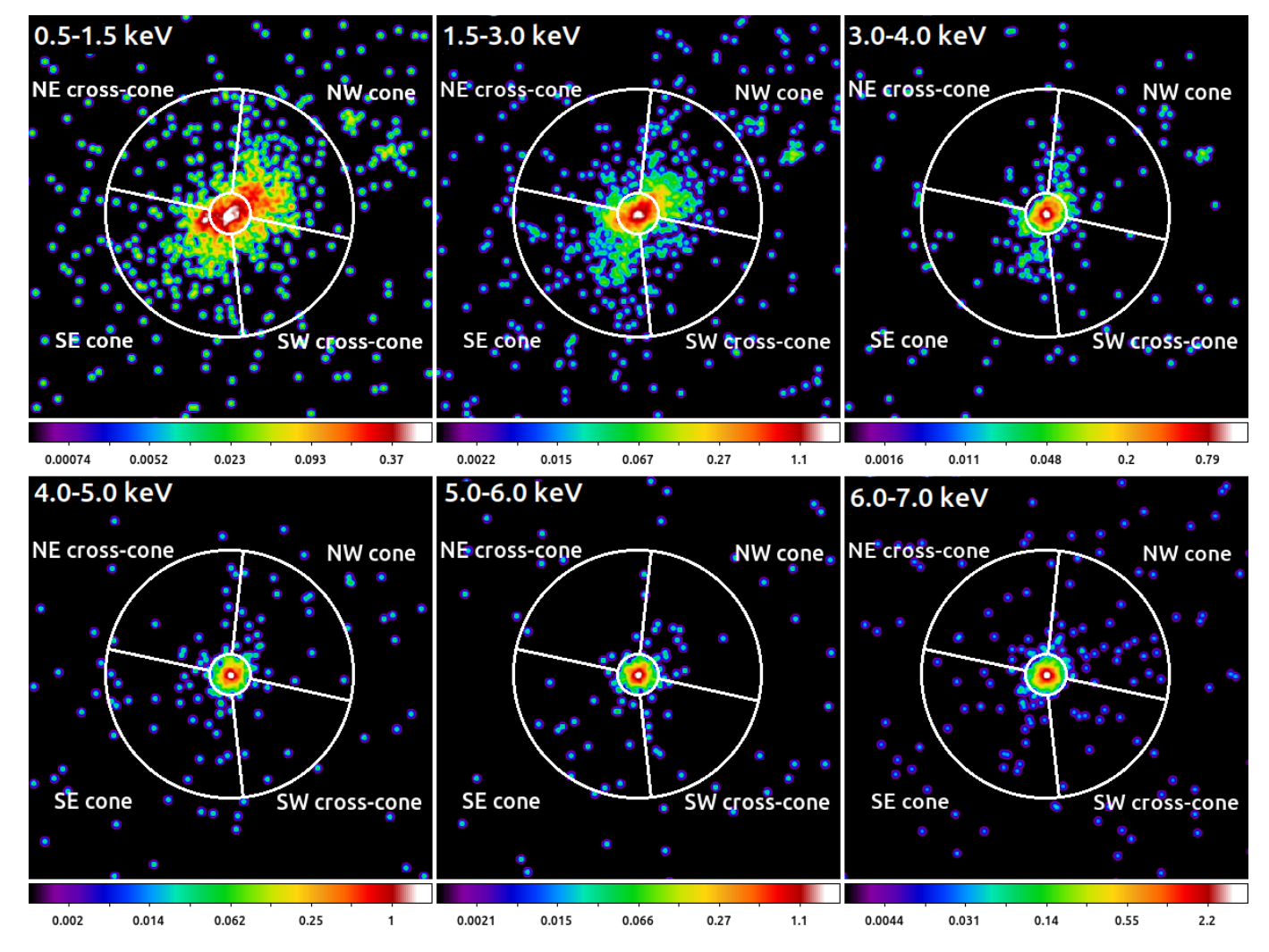


Figure 3. Images of ESO 137–G034 in different energy bands, starting from the left-top corner: $0.5-1.5 \,\mathrm{keV}$, $1.5-3.0 \,\mathrm{keV}$, $3.0-4.0 \,\mathrm{keV}$, $4.0-5.0 \,\mathrm{keV}$, $5.0-6.0 \,\mathrm{keV}$, and $6.0-7.0 \,\mathrm{keV}$. Contours mark the spectral extraction regions. The images were binned to $1/8 \,\mathrm{px}$ resolution and smoothed using a Gaussian kernel with $\sigma = 2 \,\mathrm{px}$.

The same regions were used to extract the PSF radial profiles, which were normalized to match the number of counts in the inner 1.5'' central region. In Fig. 4, we present the background-subtracted radial surface brightness profiles for both the data and PSF. Table 2 shows the excess of counts in the data over the PSF for the cone and cross-cone regions across energy bands. From 0.5 to 3 keV, both cone regions show highly significant extended surface brightness (> 14σ). In the $3.0-4.0 \,\mathrm{keV}$ range, the surface brightness is extended at $> 5 \sigma$ significance. In 4–5 keV energy range, only the SE cone shows extended emission with a significance $> 3\sigma$. There is no significant extension in the 5-6 keV band. In the 6-7 keV range, the presence of extended emission is confirmed at the $\sim 3\sigma$ level in the NW cone and at the $\sim 2\sigma$ level in the SE cone. The cross-cone regions show extended emission with $> 5\sigma$ significance up to 3 keV, after which

the radial profiles become consistent with the nuclear PSF.

4. SPECTRAL ANALYSIS

4.1. Extraction of Spectra

Source and background energy spectra were extracted separately for each observation. We used a circular region for the nucleus $(r_N=1.5'')$ and panda regions with inner radius $r_{\rm in}=1.5''$ and outer radius $r_{out}=9''$ for the cone and cross-cone regions, using the same position angle definitions as in Sec. 3.2.2. Point sources identified with the wavdetect tool were excluded. For the background, we used a concentric panda region with $r_{\rm in}=10''$ and $r_{\rm out}=12''$, excluding two point sources at that radius. The spectra were combined using the combine_spectra script, and in all cases, the background was subtracted before modeling.

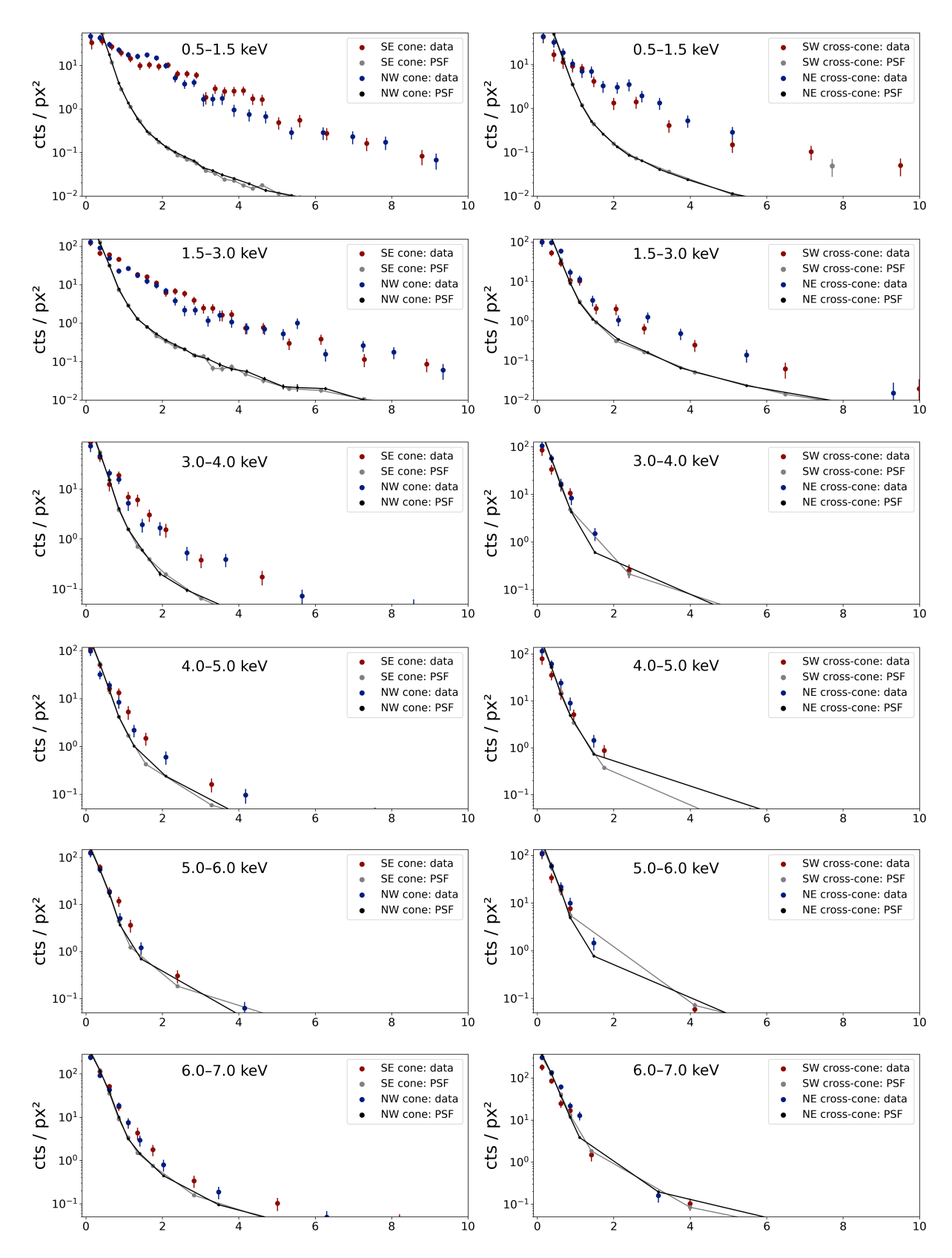


Figure 4. Background-subtracted surface brightness radial profiles in the cone regions (left column) and cross-cone regions (right column) with corresponding PSF profiles, for different energy ranges, from the top to the botom: $0.5-1.5 \,\mathrm{keV}$, $1.5-3.0 \,\mathrm{keV}$, $3.0-4.0 \,\mathrm{keV}$, $4.0-5.0 \,\mathrm{keV}$, $5.0-6.0 \,\mathrm{keV}$, and $6.0-7.0 \,\mathrm{keV}$. Error bars correspond to 1σ confidence intervals.

Initially, spectra from the two cone regions were extracted and fitted independently. As the best-fit model parameters were consistent within uncertainties, we combined the spectra from both cones to improve data statistics. The same procedure was followed for the cross-cone regions, where photon statistics are even more limited.

4.2. Spectral Models

Spectral fitting was performed with Sherpa v4.16.0 (Siemiginowska et al. 2024). Fit quality was assessed based on the χ^2 statistic, with variance calculated from the data² and the presence of significant localized residuals (Fabbiano et al. 2018). Data were binned with a minimum of 10 counts per bin. Fits were performed in the 0.3–7.0 keV energy range. All provided errors represent 1σ confidence intervals, calculated with the conf () function implemented in sherpa. Unless specified otherwise, results and definitions are provided in cgs units.

To model the photoionized spectra, we constructed a grid of models using Cloudy c.23.01 (Gunasekera et al. 2023). Following Kraemer et al. (2020), we assumed an incident radiation field in the form of a broken power-law, $L \propto \nu^{\alpha_i}$, with $\alpha_1 = 1.0$ for $h\nu \in (10^{-4}, 13.6)\,\mathrm{eV}$, $\alpha_2 = 1.3$ for $h\nu \in (13.6, 500)\,\mathrm{eV}$, and $\alpha_3 = 0.5$ for $h\nu \in (0.5, 300)\,\mathrm{keV}$ and $1.5\times$ solar abundance. We assumed a turbulent velocity of $100\,\mathrm{km}\,\mathrm{s}^{-1}$ and a hydrogen density of $10^{4.5}\,\mathrm{cm}^{-3}$. The grid spanned the range $\log U = [-2, 2]$ and $\log N_H = [21, 25]$ with a step size of 0.1. U is the dimensionless ionization parameter defined as $\frac{\Phi(H)}{cn(H)}$, the ratio of ionizing photons flux $\Phi(H)$, and the total hydrogen density n(H), with c marking the speed of light. $\log N_H$ is a common logarithm of the hydrogen column density in atoms per cm² units.

The spectral models also included xsapec and xszphabs, which are xspec (Arnaud et al. 1999) implementations of the Astrophysical Plasma Emission Code (APEC, Smith et al. 2001) and photoelectric absorption (Balucinska-Church & McCammon 1992) models. xsapec parameters include plasma temperature, kT, abundance, redshift, and normalization, norm, in norm_a = $\frac{10^{-14}}{4\pi D_A^2(1+z)^2} \int \mathrm{d}V \, n_e n_H$ units. D_A denotes the angular diameter distance to the source, n_e and n_H are the electron and ion densities, and $\mathrm{d}V$ is the volume element. Two other model parameters-redshift, z, and metallicity-were frozen at the source redshift and solar metallicity, respectively. xszphabs is described by the equivalent hydrogen column density, N_H , and redshift, z.

Additionally the mytorus model was employed to describe the torus-reprocessed nuclear emission (Yaqoob 2012). We included Compton-scattered power-law continuum and fluorescent Fe $K\alpha$ line emission components. Model parameters include intrinsic continuum photon index, Γ , component normalization, norm, defined as photon flux at 1 keV, equatorial column density N_H , inclination angle between the torus polar axis and the observer's line of sight in degrees, and redshift.

For the soft X-ray emission, we tested several model combinations: a single xsapec, a single cloudy, a combination of both, and models with two xsapec or two cloudy components. Galactic absorption was always included via the xsphabs component, with a fixed hydrogen column density of $N_H = 2.36 \times 10^{20} \, \mathrm{cm}^{-2}$ (HI4PI Collaboration et al. 2016). Presence of a second xsphabs component was tested to account for the intrinsic absorption.

4.3. Fitting Results 4.3.1. Nucleus

The best-fit model for the nuclear spectrum consists of two cloudy components with an internal absorption, xsphabs, and a mytorus component. Single apec and single cloudy models do not provide satisfactory fit to the data (see Appendix A for the f-test results). The soft part of the spectra can also be described by a combination of apec and cloudy, with slightly worse fit statistics ($\chi^2 = 1.07$ and $\chi^2 = 1.18$, respectively) and apec best-fit temperature $kT \sim 0.1 \, \text{keV}$. This model can be however rejected based on the unrealistically high intrinsic luminosity of the apec component ($\sim 10^{44} \text{erg}$ s^{-1} in $0.05 - 4 \,\text{keV}$ energy range). A combination of two thermal components leads to poorer fit quality, with $\chi^2 = 1.23$ (see Appendix A). During the fitting procedure, we fixed the inclination angle in the mytorus model to 80°, as appropriate for a CT AGN in which the torus is blocking our view of the central AGN, and set the intrinsic continuum photon index for both the continuum (c index) and line components (Fe index) to $\Gamma = 1.8$, a typical value for AGN (e.g., Marchesi et al. 2017). The equatorial column densities $(N_{HFe} \text{ and } N_{Hc})$, the normalization of the fluorescent Fe line $(norm_{Fe})$, and the normalization of the contin $uum (norm_c)$ were treated as free parameters.

The fitted parameters of the cloudy models include ionization parameter (log U) the gas column density (log N_H) and the normalization. The soft emission (< 4.0 keV) is dominated by a combination of a highly ionized, low-column-density component (log $U_h \sim 0.6$, log $N_{Hh} \sim 19$) that dominates below 1 keV, and a low-

² chi2datavar, see https://cxc.cfa.harvard.edu/sherpa/statistics/ index.html#chidata

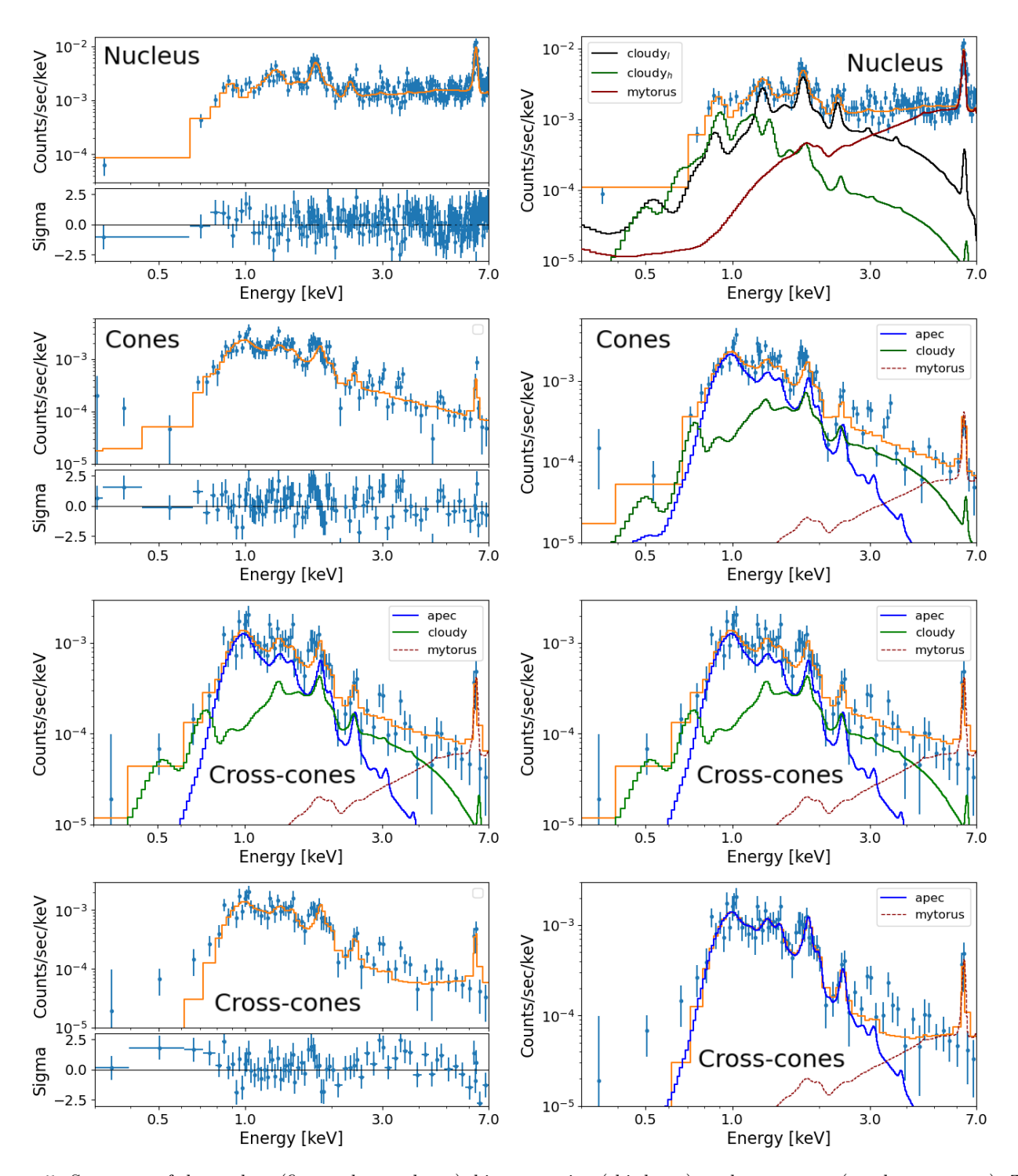


Figure 5. Spectrum of the nucleus (first and second row), bi—cone region (third row), and cross-cones (two bottom rows). The left column shows the best-fit model and its residuals, while the right column presents the components of the best-fit models.

ionization, high-column-density component ($\log U_l \sim -1.3$, $\log N_{Hl} \sim 22$), that dominates in the feature-rich $1-3\,\mathrm{keV}$ band. As the best-fit of the intrinsic absorption gives only an upper limit on the equivalent column density ($N_H < 3 \times 10^{20}\mathrm{atoms~cm^{-2}}$), we removed it from the final model. We denote ionized, low-column-density cloudy component with h and low-ionization, high-column-density cloudy component with l.

The hard X-ray emission ($>4\,\mathrm{keV}$) is dominated by the Compton-scattered component from mytorus, with comparable equatorial column densities and normalizations for both the line and continuum components. The iron line and continuum emission are absorbed by column densities that are compatible within errors. An additional absorbed power-law model component, which would account for the transmitted continuum, does not improve the fit statistics

4.3.2. Bi-cones

Based on the PSF simulations (Sec. 3.2.1), we expect the bi-cone emission to dominate over the nuclear PSF leakage at energies below $4\,\mathrm{keV}$. There is also extended emission present in the $6\text{--}7\,\mathrm{keV}$ band. To account for the nuclear PSF contamination in the bi-cone spectra above $4\,\mathrm{keV}$, we added a mytorus component to each model, with parameters fixed to the best-fit values obtained for the nucleus, freezing the normalization of these components to $\sim 4\%$ of the nuclear values. 4% is the contribution of the hard PSF to the radii > 1.5'', estimated from the our simulated PSF (see Fig. 4). This mytorus component is associated with instrumental effects and is not the actual characteristics of the diffuse emission.

Initially, we fit the spectra of the two cones separately; however, due to the limited photon statistics, the bestfit model parameters were not well constrained and are consistent with each other within the errors. Therefore, we merged the spectra of the NW and SE cones. We initially allowed for intrinsic absorption (xsphabs), but the resulting best-fit column density was only an upper limit, so this component was excluded in the final model. Single apec and single cloudy models do not provide satisfactory fit to the data (see Appendix A for the f-A model consisting of a combination test results). of apec and cloudy components leads to the best fit quality, with $\chi^2 = 1.37$. Models with two apec and two cloudy components provide poorer fits, with $\chi^2 = 1.54$ and $\chi^2=1.78,$ respectively. The apec + cloudy model is also preferred based on the fit residuals. The cloudy model fails to reproduce the spectral shape around \sim 1 keV, corresponding to the position of the Ne IX, Ne X,

and Fe-L line blend (see the bottom panel of Fig. A1), which is well reproduced by the apec model. The purely thermal model, on the other hand, performs worse in describing the shape of the spectrum at energies between 1.5 and $4.0\,\mathrm{keV}$.

Introducing an additional component to the apec and cloudy combination does not improve the fit quality. In our resulting fit, the thermal plasma has a best-fit temperature of $kT \sim 1.0 \,\mathrm{keV}$, and the photoionized gas is characterized by moderate ionization (log $U \sim 0$) and low column density (log $N_H \sim 20.8$). Best-fit values of parameters are included in Tab. 3.

Consistent with the PSF modeling, the continuum emission above $4\,\mathrm{keV}$ is well described by a mytorus component fixed at the expected $\sim 4\%$ of the nuclear normalization. The extended emission detected in one of the cones at $6-7\,\mathrm{keV}$ energy range is modeled by an iron line included in the cloudy model.

Below $1.5\,\mathrm{keV}$ the emission is dominated by the apec model, while in the $1.5-2.5\,\mathrm{keV}$ energy range apec and cloudy emission are comparable, and above $2.5\,\mathrm{keV}$ cloudy dominates.

In $0.3-4.0\,\mathrm{keV}$ energy range, the de-absorbed luminosity of the thermal plasma emission is $\sim 9.07\times 10^{39}\,\mathrm{erg\,s^{-1}}$, comparable with the de-absorbed luminosity of the photoionized gas emission $\sim 1.06\times 10^{39}\,\mathrm{erg\,s^{-1}}$.

4.4. Cross-cones

As in the bi-cone region, we account for nuclear PSF leakage by adding a mytorus component with best-fit parameter values describing the nuclear emission and normalization fixed at $\sim 4\%$ of the nuclear value (based on PSF modeling).

Spectra extracted from the cross-cone region have significantly lower count statistics. While a single model component can result in a statistically satisfactory fit, it produces correlated residuals. Therefore, we present also a two-component model consisting of both apec and cloudy. Parameters describing the thermal plasma are well constrained, with a best-fit temperature of $kT \sim 0.95 \, \mathrm{keV}$, such that the apec component dominates emission from $0.7-2 \, \mathrm{keV}$. Adding the cloudy component does not improve fit statistics significantly, but it removes the correlated fit residuals (see Tab. 3).

5. DISCUSSION

5.1. The nuclear region

As discussed in Sec. 4.3.1 and shown in Fig. 5, the spectrum of the nuclear region below 4 keV, where the direct AGN contribution is likely to be minimal because ESO 137-G034 is a CT AGN, can be mod-

Table 3.	Spectral	fitting	results
----------	----------	---------	---------

Region	Component	Parameter	Value $\pm 1\sigma$ error	Units
	*			Units
Nucleus	\mathtt{cloudy}_l	$\log U_l$	$-1.41^{+0.42}_{-0.31}$	_
${ t cloudy}_h$ + ${ t cloudy}_l$ + ${ t mytorus}$		$\log N_{Hl}$	$22.17^{+0.50}_{-0.25}$	$\log(\text{atoms cm}^{-2})$
Reduced $\chi^2 = 1.05$		norm_l	$4.92^{+1.48}_{-4.00}$	$10^{-14} \times \text{photons cm}^{-2} \text{s}^{-1}$
	\mathtt{cloudy}_h	$\log U_h$	$0.54^{+0.23}_{-0.18}$	_
		$\log N_{Hh}$	$19.34^{+0.57}_{-0.33}$	$\log(\text{atoms cm}^{-2})$
		norm_h	$1.61^{+1.32}_{-1.17}$	$10^{-14} \times \text{photons cm}^{-2} \text{s}^{-1}$
	mytorus	N_{Hc}	$2.0^{+1.85}_{-0.60}$	$10^{24} \times \text{atoms cm}^{-2}$
		$\mathrm{norm}_{\mathbf{C}}$	$1.15^{+0.76}_{-0.40}$	$10^{-2} \times \text{photons cm}^{-2} \text{s}^{-1}$
		N_{HFe}	$1.75^{+0.18}_{-0.32}$	$10^{24} \times \text{atoms cm}^{-2}$
		$_{ m norm}_{ m Fe}$	$1.50^{+0.26}_{-0.31}$	$10^{-2} \times \text{photons cm}^{-2} \text{s}^{-1}$
Cone Region	cloudy	$\log U$	$-0.50^{+0.07}_{-0.66}$	_
${\tt xsapec}$ + ${\tt cloudy}$ + ${\tt mytorus}^a$		$\log N_H$	$20.28^{+0.19}_{}$	$\log(\mathrm{cm})^{-2}$
Reduced $\chi^2 = 1.37$		norm	$3.38^{+1.68}_{-0.86}$	$10^{-14} \times \text{photons cm}^{-2} \text{s}^{-1}$
	xsapec	kT	$0.93^{+0.37}_{-0.37}$	keV
		norm	$1.49^{+0.14}_{-0.12}$	10^{-5}norm_a
Cross-Cone Region	xsapec	kT	$0.95^{+0.08}_{-0.10}$	keV
${\tt xsapec}$ + ${\tt cloudy}$ + ${\tt mytorus}^a$		norm	$8.63^{+0.95}_{-0.91}$	10^{-6} norm_a
Reduced $\chi^2 = 0.55$	cloudy	$\log U$	$-0.80^{+0.34}_{-0.68}$	-
		$\log N_H$	$20.00^{+0.63}_{}$	$\log(\text{atoms cm}^{-2})$
		norm	$7.79^{+0.34}_{-68}$	$10^{-14} \times \text{photons cm}^{-2} \text{s}^{-1}$
${ t xsapec}$ + ${ t mytorus}^a$	xsapec	kT	$0.90^{+0.07}_{-0.05}$	keV
Reduced $\chi^2 = 1.15$		norm	$1.89^{+0.20}_{-0.22}$	$10^{-5} \times \text{photons cm}^{-2} \text{s}^{-1}$

^a mytorus accounts for the PSF leakage from the nucleus. Its normalization is fixed to 4% of the nucleus normalization.

eled as emission of at least two photoionized gas phases, a highly ionized, low-column-density component $(\log U_h \sim 0.5, \log N_{Hh} \sim 19)$ and a low-ionization, highcolumn-density component (log $U_l \sim -1.6$, log $N_{Hl} \sim$ 22). In Fig. 6, we compare the best-fit ionization values for ESO 137-G034 with different CT AGN where a two-component cloudy best-fit model has been reported in the literature: ESO 138-G001 (De Cicco et al. 2015), ESO 428-G001 (Fabbiano et al. 2018), IC 5063 (Travascio et al. 2021), Mrk 573 (Paggi et al. 2012), NGC 1068 (Kraemer et al. 2015), NGC 3783 (Blustin et al. 2002), NGC 5728 (Trindade Falcao et al. 2023), and NGC 7212 (Jones et al. 2020). Fig. 6 shows that the ionization parameters we find for ESO 137-G034 are consistent with the relation between the high and low ionization parameters obtained for other CT AGN. These results suggest at least two-phase photoionized medium in the extended emission components of CT AGN, probably arising from a distribution of densities in the ISM of the circum-nuclear region.

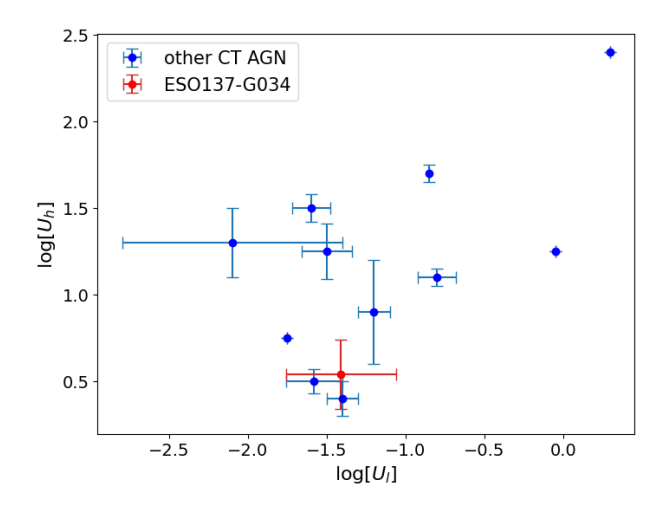


Figure 6. Best-fit ionization of two cloudy components fitted to the nucleus (r < 1.5'') spectra, for ESO 137-G034 and other CT AGN (see Sec. 5.1 for reference).

The high-energy part of the nuclear spectrum is described well by the mytorus, that models the CT AGN emission where photons from the inner accretion disk

and corona are intercepted by the nuclear torus, which gives rise to the reflection spectral component and the fluorescent Fe K α 6.4 keV line.

5.2. The extended spectrally complex bi-cones

As shown in Sec. 3, there is a strong extended X-ray emission in ESO 137-G034, displaying the characteristic dual ionization cone morphology commonly observed in Seyfert 2 galaxies. Extended emission in the bi-cone region is detected at energies up to 5 keV and additionally in the 6–7 keV range, which includes the Fe K α emission line. In the soft energy band (< 3.0keV) this extended bi-cone emission is detected as far as 2 kpc from the nucleus, while at higher energies reaches \sim 800 pc (Fig. 4). The azimuthal profiles of the extended emission show an energy-dependent morphology, with SE cone exhibiting different emission maxima in the 0.3–1.5 keV and 1.5–4.0 keV energy ranges (Fig. 2).

Spectral analysis (Sec. 4) showed that the extended emission in the bi-cones is multicomponent, with signatures of both shock-heated thermal and photoionized plasma emission.

The best-fit model describing the soft part of the bicone spectrum is apec + cloudy. Even though the photon statistics and CCD's energy resolution limit our abilities to characterize unequivocally the parameters of the emitting gas, based on the spectral fitting results, we can conclude that the extended emission originates from a mixture of a shock-heated thermal plasma and a photo-ionized medium. As shown in Table A1, a two cloudy model or a two apec model give a bad fit and therefore are rejected. Thermal plasma emission in particular is needed to account for the spectral shape up to $\sim 1 \,\mathrm{keV}$. Based on the best-fit model, we conclude that hot plasma emission dominates the soft energy band (especially between 0.8 and 1.5 keV), and photo-ionized gas is equally important between 1.5 keV and 2.5 keV, while it dominates between 2.5 keV and 4.0 keV (see Fig. 5).

From the temperature of the thermal component, we estimated the velocity of the associated shock as $v \sim 800-1000\,\mathrm{km\,s^{-1}}$ ($v=\sqrt{\frac{16kT}{3\mu}}$, where k is the Boltzmann constant and μ is the mean molecular mass of a fully ionized gas; e.g., Fabbiano et al. 2018).

A single cloudy component describing the photoionized plasma emission in the cone region can be a major simplification. Due to the size of the region, the ionization parameter value may be different at different distances from the nucleus. This effect, however, depends on the ISM density profile and is mitigated if the density follows $\propto r^{-2}$, a slope often found in AGN winds (Bianchi et al. 2006). To spatially disentangle thermal and photo-ionized emission regions, we conducted a spatial analysis of the energy-dependent emission morphology.

5.2.1. The [O III]/ X-ray ratio diagnostic

Our first approach is to examine the radial profile of the [O III] to soft X-ray flux ratio in different spatial regions. This ratio is a proxy of the ionization parameter for a photo-ionized gas, and is expected to have an approximately power-law shape (Bianchi et al. 2006). In the case of photoionized AGN winds, the [O III]/X-ray ratio is expected to be constant, given the $\propto r^{-2}$ radial dependence of both the ionizing flux and the gas density. This radially constant [O III]/X-ray ratio has been observed in NGC 4151 (Wang et al. 2009, 2011b).

We investigated the relation between [O III] (Ferruit et al. 2000) and the $0.3-3.0\,\mathrm{keV}$ X-ray morphology in the ESO 137-G034 bi-cone region. Following the approach of Paggi et al. (2012), we used a conversion factor of 4.6×10^{-12} , based on the spectral modeling of the cone emission, to convert cts s⁻¹ to **erg cm**⁻² s⁻¹.

We used the entire SE and NW cone regions, and the subregions, marked in blue and red, which were chosen based on the positions of the double peaks in the azimuthal profile of the SE cone emission, appearing in the soft and medium energy ranges respectively (see Fig. 2 in Sec. 3.1). These subregions are defined by the position angles: $170^{\circ} - 215^{\circ}$ - blue part of the SE cone, $230^{\circ} - 260^{\circ}$ - red part of the SE cone.

The [O III]/X-ray profiles extracted for the full NW and SE cone regions and the sub-regions are plotted in the left panel of Fig. 7. In the SE cone, the full cone profile (in black) has a lower [O III]/X-ray ratio in the inner 3" ($\sim 600 \,\mathrm{pc}$). A similar [O III] decrement is only observed in the inner $\sim 1''$ ($\sim 200\,\mathrm{pc}$) of the NW cone (plotted in grey). This lower ratio suggest the presence of additional non-photoionized (i.e. thermal) X-ray emission (see Wang et al. 2009). At larger radii (> 3"), the [O III]/X-ray ratio for the SE cone (black points) and NE cone (grey points) are constant, consistent with the expectations from photoionized wind emission. However, the situation appears more complex if we examine the red and blue subregions of the SE cone. The [O III]/X-ray profile behaves different, with ratio increasing between 1'' and 3'' for the red region and decreasing for the blue region, suggesting a more complicated spatial distribution of different parameters describing the emission, e.g., relative contributions of shock-heated thermal and photoionized plasma components, plasma temperature or absorption.

5.2.2. X-ray spectral band ratio imaging

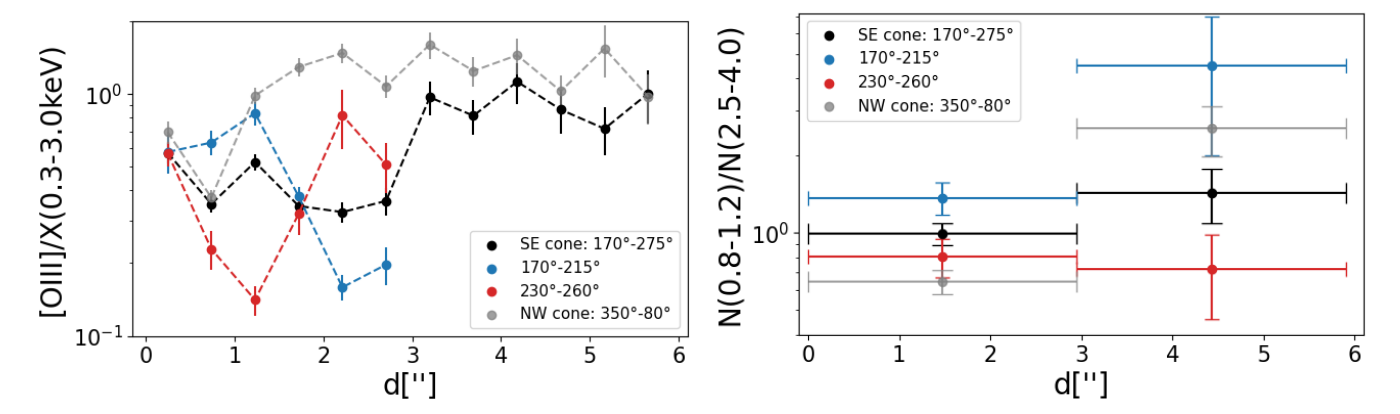


Figure 7. Left panel: O[III]/X(0.3-3.0 keV) flux ratio for the SE cone (black points), NW cone (grey points) and two regions within SE (red and blue, corresponding to cones marked in red and blue in Fig. 2. Right panel: The X-ray hardness ratio for SE cone (black points), NW cone (grey points) and two regions within SE, red and blue (see Fig. 7).

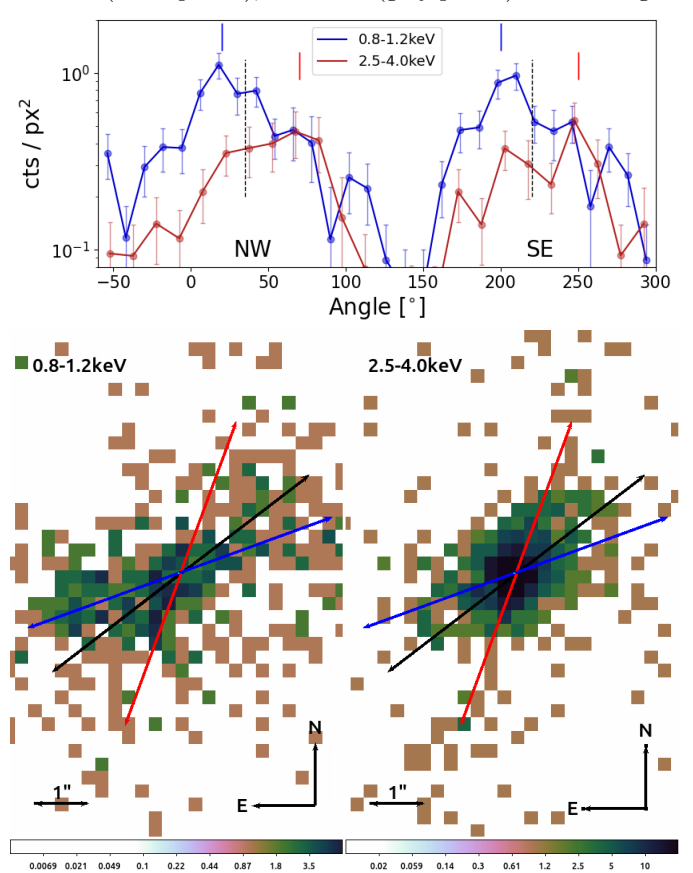


Figure 8. Lower panel: images of ESO 137-G034 in energy bands energy bands dominated by apec $(0.8-1.2\,\mathrm{keV}$, left panel) and cloudy $(2.5-4.0\,\mathrm{keV})$, right panel). Images were binned to 0.5 of the original *Chandra* pixel size. Upper panel: azimuthal profiles of the extended emission between 1.5" and 9.0" from the nucleus for corresponding energy ran in bi-cone spectra. The red and blue vertical lines mark maxima of azimuthal profiles. Their angular position are marked in lower panels. The black lines mark the positions of the maximum for $0.3-7.0\,\mathrm{keV}$ energy range.

The ACIS CCD resolution, coupled with the exquisite Chandra imaging capabilities can be used to explore spectrally different features in the extended X-ray emission (Wang et al. 2011a; Paggi et al. 2012; Fabbiano et al. 2018). We follow this approach here, using the spectral fit results to define energy bands dominated by either thermal or photoionized emission.

Using the best-fit model for spectrum of the combined cone emission (Fig. 5) as a guide, we select spectral bands where the two different emission models dominate. For the thermal emission of shock-heated plasma, we choose the $0.8-1.2\,\mathrm{keV}$ band, where the thermal contribution exceeds the photoionization contribution by a factor of ~ 10 . This band includes the Ne IX, Ne X, and Fe-L emission (Wang et al. 2011a). For the photoionized contribution we use the $2.5-4.0\,\mathrm{keV}$ band, where the cloudy contribution is dominant.

The right panel of Fig. 7 presents the radial profile of X-ray hardness ratio, defined as N(0.8-1.2)/N(2.5-4.0), where N(0.8-1.2) and N(2.5-4.0) are a number of counts in $0.8-1.2\,\mathrm{keV}$ and $2.5-4.0\,\mathrm{keV}$ energy ranges respectively. Profiles are plotted for full SE (black) and NW (grey) cones and SE cone subregions (blue and red, see bottom-right panel of Fig. 2). In the inner part of the source ($<3''\sim600\,\mathrm{pc}$) the hardness ratio is higher in the SE cone (black points) than in NW cone (grey points). The excess originates from the SE subregion marked in blue, suggesting a higher contribution of shock heated thermal plasma emission in that part of the source.

To further examine the spatial separation of the thermal and photoionized emission, based on our spectral modeling results, we extracted azimuthal profiles (upper panel of Fig. 8) for the soft and medium energy bands, as previously done in Sec. 3.1. This time, following the spectral fitting results, we adjusted the energy ranges to

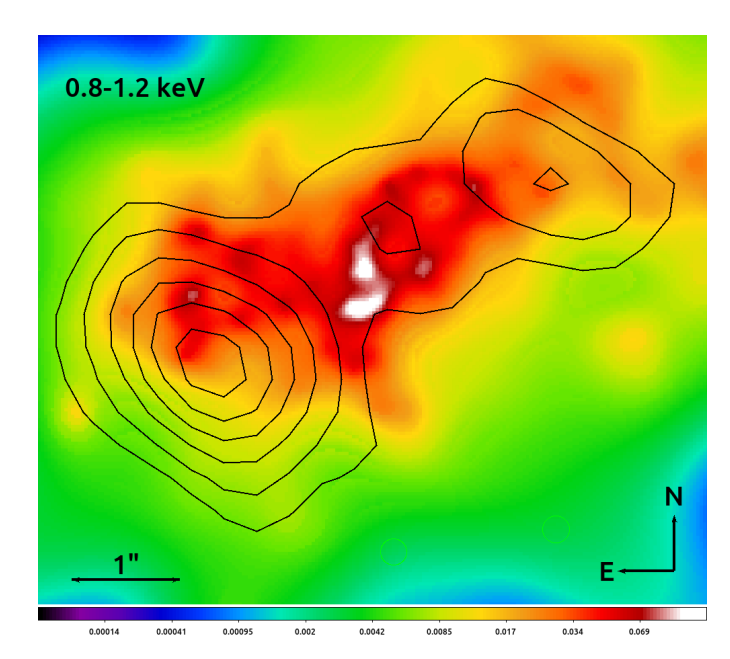


Figure 9. Adaptively smoothed X-ray image of ESO 137-G034 in the $0.8-1.2\,\mathrm{keV}$ energy band. The 3 cm radio jet emission (Morganti et al. 1999) is marked with black contours.

0.8–1.2 keV and 2.5–4.0 keV. This revealed a clear offset of the soft (blue) emission maxima, located at $\sim 20^{\circ}$ and $\sim 200^{\circ}$, from the maxima determined using the full energy range (0.3–7.0 keV), located at $\sim 35^{\circ}$ and $\sim 215^{\circ}$ (vertical dashed lines), not only in the SE cone but also in the NW cone. The azimuthal profile for the 2.5-4.0 keV energy band (red) more closely resembles that of the full energy band, but shows hints of a maxima offset in the opposite direction to the soft-band emission at $\sim 70^{\circ}$ and $\sim 250^{\circ}$. This energy dependence in the direction of the emission extension is also visible in the images. In the lower panel of Fig. 8 we present images of the ESO 137-G034 X-ray emission in $0.8-1.2 \,\mathrm{keV}$ (left) and $2.5 - 4.0 \,\mathrm{keV}$ (right) energy ranges binned with the 0.5 original Chandra pixel size, with lines marking the positions of the maxima in the azimuthal profiles.

5.2.3. Radio jet emission

In Fig. 9 we compare the $0.8-1.2\,\mathrm{keV}$, thermal emission dominated image, with the position of the 3 cm radio jet of ESO 137-G034 from the Australia Telescope Compact Array (ATCA, half-power beam width = 1.271'' Morganti et al. 1999). Contour levels start at the 3σ level, where σ is the standard deviation of the background-dominated region, and increase by a factor of $\sqrt{2}$. The radio jet aligns well with the structure of the extended X-ray emission. It is particularly pronounced in the SE cone region, extending up to $\sim 3''$ ($\sim 600\,\mathrm{pc}$) from the nucleus, in the area associated with

the [O III]/X-ray ratio decrement (Fig. 7) and the soft emission excess seen in the X-ray hardness ratio map (Fig. 8). This suggests that the thermal emission component may arise from the shocks induced by the propagation of the radio jet, further reinforcing the conclusion of a strong shock presence in the SE cone. The presence of strong shocks in this regions is also confirmed by the optical *HST* ionization map (Król et al., submitted). The difference can be also partially associated with the extinction of the [O III] emission due to the dust.

The stronger shock presence in the SE cone would be consistent with findings of Zhang et al. (2024a), who studied regions roughly corresponding to the inner part SE and NW cones defined in our analysis through polycyclic aromatic hydrocarbon (PAH) diagnostics. The SE cone appears to have a lower fraction of small and neutral grains compared to the NW cone and the nucleus. Since small, ionized PAHs are most vulnerable to destruction, this indicates differing environmental conditions. Moreover, Zhang et al. (2024b) report strong shock signatures in ESO 137-G034 based on broad emission line profiles, with line widths containing the central 80% of the flux, W80 $\gtrsim 500\,\mathrm{km~s^{-1}}$) for [Ar II,III], [Ne II,III,V] and [S IV].

Assuming that shock-heated thermal plasma emission dominates the X-ray emission in the vicinity of the SE radio jet, we extracted the spectra from the part of the SE cone corresponding to the radio-jet position and the dip in the [OIII]/X-ray flux ratio, between 1.5" and 3.5" to study its physical parameters.

As in Sec. 4, we fitted the extracted spectrum with a apec+cloudy model. kT and $\log U$ were frozen at the best-fit values obtained in Sec. 4, and only model normalizations were allowed to vary. We obtained a fit characterized by $\chi^2=1.27,$ with the best-fit apec norm= $(1.28\pm0.23)\times10^{-5}~{\rm norm}_a.$ Assuming that the emitting region is cone-shaped, with the main axes on the plane of the sky and is filled with ionized hydrogen, we derive the gas density $n_H\sim0.27f^{-0.5}~{\rm cm}^{-3},$ leading to an emitting gas mass of $\sim 8\times10^5f^{0.5}~{\rm M}_\odot,$ where f marks the fraction of the thermal emitting matter within the total region volume (f<1). The pressure $p=n_HkT$ is estimated as $\sim 4\times10^{-10}f^{-0.5}$ dyn cm $^{-2},$ and the internal energy $\epsilon_{int}=1.5pV\sim2\times10^{53}f^{-0.5}$ erg.

Assuming the emitting plasma constitutes a radio jet cocoon, and that all the kinematic energy transported by the jet during its lifetime is converted at the jet head (terminal shock) into the cocoon's internal pressure, we can estimate the jet power, L_j , from $\epsilon_{\rm int} = 1.5 pV = L_j t$, where t is the jet lifetime (Stawarz et al. 2008). Assuming a jet expansion velocity of 0.3c, a value typical for Compact Symmetric Objects (CSOs) with sizes $\lesssim 500 \,\mathrm{pc}$

(as the jet of ESO 137-G034, An & Baan 2012) and assuming $\epsilon_{\rm int} \sim 2 \times 10^{53} f^{-0.5}$ erg from the X-ray spectral fitting, we estimate a lower limit to the jet power of $L_j \sim 10^{42} \sqrt{f} \, {\rm erg \, s^{-1}}$, far below the $\sim 10^{44} \, {\rm erg \, s^{-1}}$ threshold required for the jet to expand beyond its host galaxy (Mukherjee et al. 2016, 2017). The inferred jet power is comparable to that modeled for the weakest CSOs (Król et al. 2024; Wójtowicz et al. 2020).

Furthermore, we estimate the jet production efficiency, η_j , as:

$$\log \eta_j = \log(L_j \eta^{-1} c^{-2}) \simeq \log (0.1 L_j L_{\text{bol}}^{-1}) \sim -2.72,$$
(1)

assuming an efficiency $\eta = 0.1$ (King 2008) and the disk bolometric luminosity from the approximation:

$$\log L_{\text{bol}} = 0.0378(\log L_X)^2 - 2\log(\log L_X) + 60.5, \quad (2)$$

where L_X is the intrinsic X-ray luminosity in the 2–10 keV energy range (Ricci et al. 2017; Ichikawa et al. 2017). The low jet production efficiency, $\log \eta_j \sim -2.72$, is comparable to that inferred for CSOs (Wójtowicz et al. 2020).

5.3. The emission mechanism of the extended cross-cone region

317

Extended emission of ESO 137-G034 is found also in the cross-cone direction (Sec. 3), up to $\sim 3\,\mathrm{keV}$. Extended emission in the cross-cone direction has been found in multiple CT AGN (see, e.g., Fabbiano et al. 2018; Jones et al. 2021). It has been explained either in terms of nuclear emission escaping through a porous torus (Nenkova et al. 2002) or as a result of the jet interaction with a dense and patchy ISM (Mukherjee et al. 2018; Fabbiano et al. 2022).

The cross-cone spectrum is adequately fitted with a single thermal component with kT $\sim 1\,\mathrm{keV}$ (Table 3). It can also be fitted with a thermal + photoionization model similar to that of the cone emission, but the small $\chi^2 \sim 0.55$ suggests overfitting. These spectral results cannot discriminate between the porous torus and jet interaction options, given the compatibility with the cone spectrum and the much more limited statistics. However, the presence of an embedded radio jet and the shock/turbulent velocities inferred in this paper and in Zhang et al. (2024b) from MIRI [N II] observations, would favor the jet interaction possibility.

6. SUMMARY

In this paper, we report the results of our analysis of the deep *Chandra* ACIS observations of ESO 137-G034. Our main findings are summarized as follows:

- Extended X-ray emission is detected with a biconical morphology up to $5\,\mathrm{keV}$ and in the $6-7\,\mathrm{keV}$ energy range. The cross-cone regions show extended emission up to $3\,\mathrm{keV}$. In the soft energy band ($<3\,\mathrm{keV}$) the emission extends out to $\sim2\,\mathrm{kpc}$, while at higher energies can be traced out to $\sim800\,\mathrm{pc}$ in the bicones only.
- The nuclear (r < 1.5" ~ 300 pc) emission below 4 keV originates from photoionized gas and can be modeled by at least two gas phases: one highly ionized with low column density, dominating the emission in the 1.5 − 4.0 keV energy range, and one low-ionization phase with higher column density, dominating the emission below 1.5 keV. Above 4 keV, reflection from a toroidal structure (modeled with mytorus) dominates. The derived ionization parameters are consistent with those obtained for other CT AGN.</p>
- Spectral modeling shows that the bi-cone emission is a mixture of both photoionized gas (radiative feedback) and shock-heated plasma (kinematic feedback), with best-fit parameters of $\log U \sim -0.6$ and $kT \sim 0.9\,\mathrm{keV}$. Both components have comparable luminosities of $\sim 9\times 10^{39}\,\mathrm{erg\,s^{-1}}$. The thermal plasma component is required to reproduce the spectral shape around $\sim 1\,\mathrm{keV}$, dominating the 0.8–1.2 keV band by a factor of ~ 10 over the photoionized contribution. In contrast, photoionization dominates the 2.5–4.0 keV band.
- The extended emission morphology is energy-dependent, with different azimuthal profile maxima for the 0.8–1.2 keV and 2.5–4.0 keV bands. This indicates that distinct physical mechanisms dominate in different regions of the source.
- The radial [O III]/X-ray flux ratio suggest that the photoionized gas is present in both cones, dominating in the NW cone at $r > 400\,\mathrm{pc}$ and in the SE cone at $r > 800\,\mathrm{pc}$. At these radii, the profile is consistent with a $\rho \propto r^{-2}$ density law, implying radiative feedback dominance far from the nucleus. Localized X-ray excesses at smaller radii indicate additional thermal emission.
- In the SE cone, an X-ray excess coincides with the radio jet. Hardness ratio maps reveal a counts excess in the 0.8–1.2 keV band (Ne and Fe-L lines) aligned with the jet, supporting a shock origin. In this region, we estimate a lower limit to the thermal plasma internal energy of $\sim 2 \times 10^{53}$ erg and a density of $\gtrsim 0.27 \, \mathrm{cm}^{-3}$, corresponding to a mass

of $\sim 8 \times 10^5 \, \rm M_{\odot}$. These results suggest kinematic feedback plays a major role within $\sim 800 \, \rm pc$, especially in the SE cone. Assuming this plasma forms a radio jet cocoon, we infer a jet power of $L_j \sim 10^{42} \sqrt{f} \, \rm erg \, s^{-1}$ and a low jet production efficiency of $\log \eta_j \sim -2.72$, values comparable to those found for the weakest Compact Symmetric Objects.

Software: CIAO v.4.16 (Fruscione et al. 2006), Sherpa (Siemiginowska et al. 2024; Doe et al. 2007; Freeman et al. 2001), MARX (Davis et al. 2012), astropy (Astropy Collaboration et al. 2013), Cloudy (Ferland et al. 2013),

Facilities: Chandra, ACTA, HST

APPENDIX

A. ALTERNATIVE SPECTRAL MODELS

In Tab. A1, we list the best-fit parameters and fit statistics of the rejected spectral models describing the emission from the nucleus, bi-cone, and cross-cone regions. A description of the model components and their parameters can be found in Sec. 4.2. In Fig. A1, we show the regions spectra along with rejected best-fit models, their residuals, and individual model components.

Single-component models describing the emission below 4 keV can be rejected for both the nucleus and bi-cone spectra with high statistical significance, based on the F-test comparison with the best-fit two-component models. For the nucleus, the significance is $\sim 10^{-25}$ and $\sim 10^{-6}$ for the comparison of single apec and cloudy models, respectively, with the two cloudy models. For the bi-cones, the significance is $\sim 10^{-6}$ for the apec model and $\sim 10^{-12}$ for the cloudy model, both with respect to the two-component cloudy + apec model.

The two apec model was rejected for the nucleus based on the χ^2 value and the presence of correlated residuals between 1 and 3 keV (see the top panels of Fig. A1). The apec + cloudy requires non realistically high intrinsic apec luminosity. The bi-cone spectra cannot be described by either two cloudy or two apec components. The two cloudy components fail to reproduce the spectral shape around $\sim 1 \, \text{keV}$, whereas the two apec components show residuals at $\sim 1.5-3.0 \, \text{keV}$ (see the second and third rows of Fig A1). The fit statistics are also better for the apec + cloudy model. The fit statistics of the single component cloudy model for the cross-cone region is significantly worse ($\chi^2 = 1.99$), than in the case of single apec model.

REFERENCES

- Adamo, A., Atek, H., Bagley, M. B., et al. 2024, arXiv e-prints, arXiv:2405.21054,
 - doi: 10.48550/arXiv.2405.21054
- An, T., & Baan, W. A. 2012, ApJ, 760, 77, doi: 10.1088/0004-637X/760/1/77
- Arnaud, K., Dorman, B., & Gordon, C. 1999, XSPEC: An X-ray spectral fitting package, Astrophysics Source Code Library, record ascl:9910.005
- Astropy Collaboration, Robitaille, T. P., Tollerud, E. J., et al. 2013, A&A, 558, A33, doi: 10.1051/0004-6361/201322068
- Balucinska-Church, M., & McCammon, D. 1992, ApJ, 400, 699, doi: 10.1086/172032
- Benson, A. J., Bower, R. G., Frenk, C. S., et al. 2003, ApJ, 599, 38, doi: 10.1086/379160
- Bianchi, S., Guainazzi, M., & Chiaberge, M. 2006, A&A, 448, 499, doi: 10.1051/0004-6361:20054091
- Blustin, A. J., Branduardi-Raymont, G., Behar, E., et al. 2002, A&A, 392, 453, doi: 10.1051/0004-6361:20020914
- Bogdán, Á., Goulding, A. D., Natarajan, P., et al. 2024, Nature Astronomy, 8, 126,
 - doi: 10.1038/s41550-023-02111-9

- Carter, C., Karovska, M., Jerius, D., Glotfelty, K., & Beikman, S. 2003, in Astronomical Society of the Pacific Conference Series, Vol. 295, Astronomical Data Analysis Software and Systems XII, ed. H. E. Payne, R. I. Jedrzejewski, & R. N. Hook, 477
- Davis, J. E., Bautz, M. W., Dewey, D., et al. 2012, in Society of Photo-Optical Instrumentation Engineers (SPIE) Conference Series, Vol. 8443, Space Telescopes and Instrumentation 2012: Ultraviolet to Gamma Ray, ed. T. Takahashi, S. S. Murray, & J.-W. A. den Herder, 84431A, doi: 10.1117/12.926937
- De Cicco, M., Marinucci, A., Bianchi, S., et al. 2015, MNRAS, 453, 2155, doi: 10.1093/mnras/stv1702
- Doe, S., Nguyen, D., Stawarz, C., et al. 2007, in
 Astronomical Society of the Pacific Conference Series,
 Vol. 376, Astronomical Data Analysis Software and
 Systems XVI, ed. R. A. Shaw, F. Hill, & D. J. Bell, 543
- Fabbiano, G., & Elvis, M. 2022, in Handbook of X-ray and Gamma-ray Astrophysics, ed. C. Bambi & A. Sangangelo, 92, doi: 10.1007/978-981-16-4544-0_111-1
- Fabbiano, G., Elvis, M., Paggi, A., et al. 2017, ApJL, 842, L4, doi: 10.3847/2041-8213/aa7551
- Fabbiano, G., Paggi, A., Karovska, M., et al. 2018, ApJ, 865, 83, doi: 10.3847/1538-4357/aadc5d
- Fabbiano, G., Paggi, A., Morganti, R., et al. 2022, ApJ, 938, 105, doi: 10.3847/1538-4357/ac8ff8

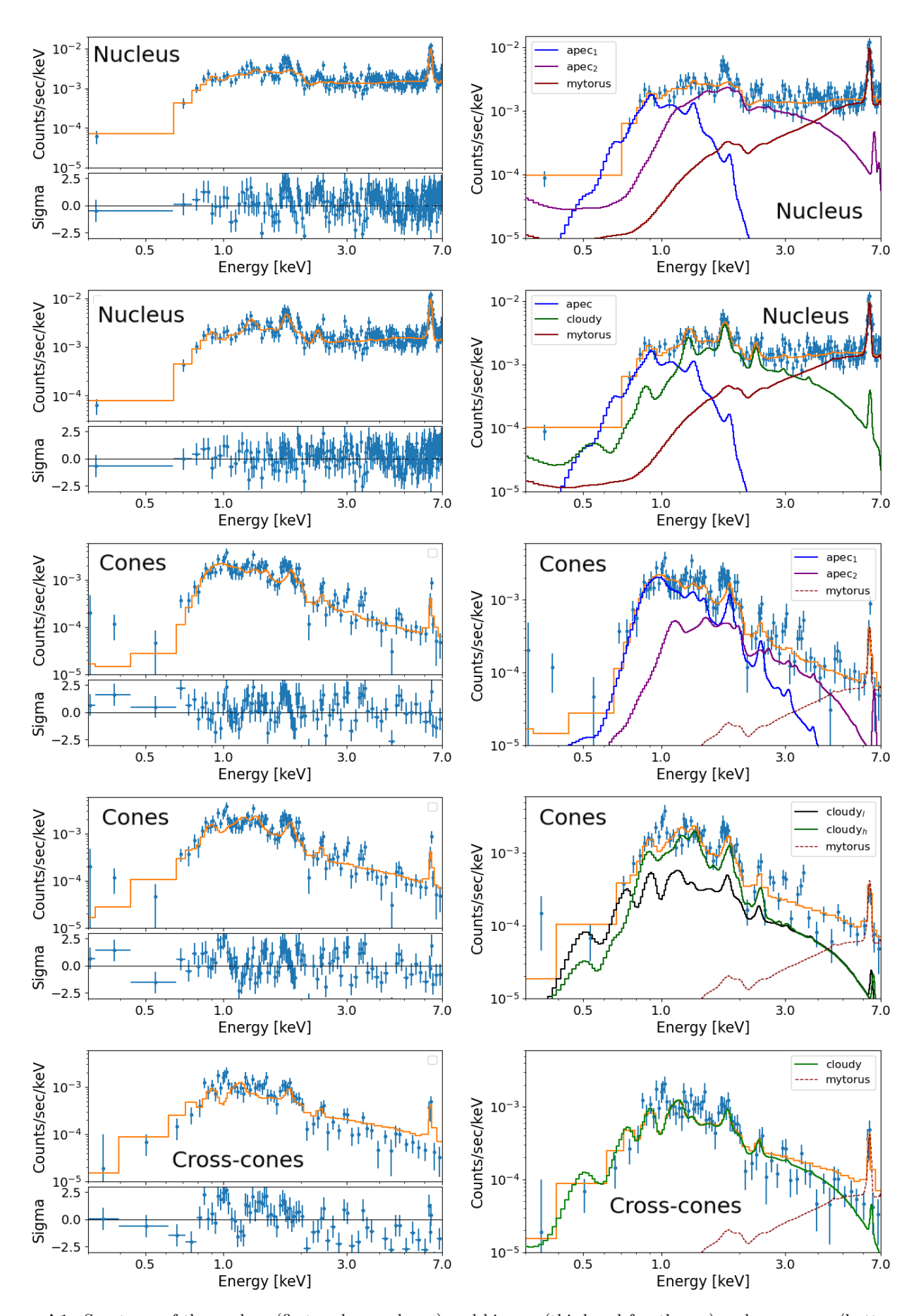


Figure A1. Spectrum of the nucleus (first and second row) and bi-cone (third and fourth row) and cross-cone (bottom row) regions. The left column shows the best-fit of rejected models and their residua, while the right column presents the model components.

Table A1. Rejected spectral models.

Region	Component	Parameter	Value $\pm 1\sigma$ errors	Units
Nucleus	${\tt xsapec}_1$	kT_1	$0.22^{+0.06}_{-0.06}$	keV
$xsphabs \times (xsapec_1 + xsapec_2) + mytorus$		$norm_1$	$2.15^{+3.60}_{-1.27}$	$10^{-4} \times \text{photons cm}^{-2} \text{s}^{-1}$
Reduced $\chi^2 = 1.24$	${\tt xsapec}_2$	kT_2	$6.97^{+}_{-1.99}$	keV
		$norm_2$	$5.45^{+1.05}_{-0.63}$	$10^{-5} \times \text{ photons cm}^{-2} \text{s}^{-1}$
	mytorus	N_{Hc}	$2.00^{+3.85}_{-1.01}$	$10^{24} \times \text{atoms cm}^{-2}$
		$\mathrm{norm}_{\mathbf{C}}$	$1.19^{+0.13}_{-0.06}$	$10^{-2} \times \text{photons cm}^{-2} \text{s}^{-1}$
		N_{HFe}	$1.49^{+0.29}_{-0.49}$	$10^{24} \times \text{atoms cm}^{-2}$
		$\mathrm{norm}_{\mathrm{Fe}}$	$1.15^{+0.31}_{-0.40}$	$10^{-2} \times \text{photons cm}^{-2} \text{s}^{-1}$
	xsphabs	N_H	$0.21^{+0.21}_{-0.19}$	$10^{22} \times \text{atoms cm}^{-2}$
$xsphabs \times (xsapec + cloudy) + mytorus$	cloudy	$\log U$	$0.25^{+0.01}_{-0.02}$	_
Reduced $\chi^2 = 1.18$		$\log N_H$	$20.10^{+0.0043}_{-0.0056}$	$\log(\text{atoms cm}^{-2})$
		norm_l	$6.86^{+0.62}_{-0.59}$	$10^{-14} \times \text{photons cm}^{-2} \text{s}^{-1}$
	xsapec	kT	$0.10^{+0.02}_{-0.01}$	keV
		norm	$1.23^{+1.37}_{-0.40}$	10^{-1}norm_a
	mytorus	N_{Hc}	$2.00^{+0.51}_{-0.32}$	$10^{24} \times \text{cm}^{-2}$
		$\mathrm{norm}_{\mathbf{C}}$	$1.18^{+0.21}_{-0.26}$	$10^{-2} \times \text{photons cm}^{-2} \text{s}^{-1}$
		N_{HFe}	$1.38^{+0.21}_{-0.21}$	$10^{24} \times \text{cm}^{-2}$
		norm_{Fe}	$1.07^{+0.17}_{-0.19}$	$10^{-2} \times \text{photons cm}^{-2} \text{s}^{-1}$
	xsphabs	N_H	$7.48^{+0.78}_{-0.82}$	$10^{21} \times \text{atoms cm}^{-2}$
Cone	${\tt xsapec}_1$	kT_1	$0.87^{+0.04}_{-0.06}$	keV
\mathtt{xsapec}_1 + \mathtt{xsapec}_2 + $\mathtt{mytorus}^a$		$norm_1$	$1.64^{+0.14}_{-0.12}$	$10^{-5} \times \text{photons cm}^{-2} \text{s}^{-1}$
Reduced $\chi^2 = 1.54$	${\tt xsapec}_2$	kT_2	$3.59^{+3.68}_{-0.97}$	keV
		$norm_2$	$9.17^{+1.66}_{-1.60}$	$10^{-6} \times \text{ photons cm}^{-2} \text{s}^{-1}$
\mathtt{cloudy}_h + \mathtt{cloudy}_l + $\mathtt{mytorus}^a$	\mathtt{cloudy}_l	$\log U_l$	$-0.25^{+0.28}_{-0.29}$	-
Reduced $\chi^2 = 1.78$		$\log N_{Hl}$	$19.8^{+2.07}_{}$	$\log(\text{atoms cm}^{-2})$
		norm_l	$2.76^{+2.16}_{-1.96}$	$10^{-14} \times \text{photons cm}^{-2} \text{s}^{-1}$
	\mathtt{cloudy}_h	$\log U_h$	$1.32^{+0.68}_{-0.04}$	_
		$\log N_{Hh}$	$20.69^{+1.34}_{-}$	$\log(\text{atoms cm}^{-2})$
		norm_h	$1.40^{+0.61}_{-1.30}$	$10^{-14} \times \text{photons cm}^{-2} \text{s}^{-1}$
Cross-Cone	cloudy	$\log U$	$-0.19^{+0.08}_{-0.04}$	-
${\tt cloudy+\ mytorus}^a$		$\log N_H$	$20.42^{+0.28}_{-0.21}$	$\log(\text{atoms cm}^{-2})$
Reduced $\chi^2 = 1.99$		norm_l	$1.48^{+1.04}_{-0.81}$	$10^{-14} \times \text{photons cm}^{-2} \text{s}^{-1}$

 $^{^{\}rm a}$ $\,$ mytorus accounts for the PSF leakage from the nucleus. Its normalization is fixed to 4% of the nucleus normalization.

- Fabian, A. C. 2012, ARA&A, 50, 455, doi: 10.1146/annurev-astro-081811-125521
- Ferland, G. J., Porter, R. L., van Hoof, P. A. M., et al. 2013, RMxAA, 49, 137, doi: 10.48550/arXiv.1302.4485
- Ferruit, P., Wilson, A. S., & Mulchaey, J. 2000, ApJS, 128, 139, doi: 10.1086/313379
- Fischer, T. C., Crenshaw, D. M., Kraemer, S. B., & Schmitt, H. R. 2013, ApJS, 209, 1, doi: 10.1088/0067-0049/209/1/1
- Freeman, P., Doe, S., & Siemiginowska, A. 2001, in Society of Photo-Optical Instrumentation Engineers (SPIE)
 Conference Series, Vol. 4477, Astronomical Data Analysis, ed. J.-L. Starck & F. D. Murtagh, 76–87, doi: 10.1117/12.447161
- Fruscione, A., McDowell, J. C., Allen, G. E., et al. 2006, in Society of Photo-Optical Instrumentation Engineers (SPIE) Conference Series, Vol. 6270, Observatory Operations: Strategies, Processes, and Systems, ed. D. R. Silva & R. E. Doxsey, 62701V, doi: 10.1117/12.671760
- Garmire, G. P., Bautz, M. W., Ford, P. G., Nousek, J. A.,
 & Ricker, Jr., G. R. 2003, in Society of Photo-Optical Instrumentation Engineers (SPIE) Conference Series,
 Vol. 4851, X-Ray and Gamma-Ray Telescopes and Instruments for Astronomy., ed. J. E. Truemper & H. D. Tananbaum, 28–44, doi: 10.1117/12.461599
- Gunasekera, C. M., van Hoof, P. A. M., Chatzikos, M., & Ferland, G. J. 2023, Research Notes of the American Astronomical Society, 7, 246, doi: 10.3847/2515-5172/ad0e75
- HI4PI Collaboration, Ben Bekhti, N., Flöer, L., et al. 2016, A&A, 594, A116, doi: 10.1051/0004-6361/201629178
- Hinshaw, G., Larson, D., Komatsu, E., et al. 2013, ApJS, 208, 19, doi: 10.1088/0067-0049/208/2/19
- Ichikawa, K., Ricci, C., Ueda, Y., et al. 2017, ApJ, 835, 74, doi: 10.3847/1538-4357/835/1/74
- Jones, M. L., Fabbiano, G., Elvis, M., et al. 2020, ApJ, 891, 133, doi: 10.3847/1538-4357/ab76c8
- Jones, M. L., Parker, K., Fabbiano, G., et al. 2021, ApJ, 910, 19, doi: 10.3847/1538-4357/abe128
- Kereš, D., Katz, N., Davé, R., Fardal, M., & Weinberg, D. H. 2009, MNRAS, 396, 2332, doi: 10.1111/j.1365-2966.2009.14924.x
- King, A. 2008, NewAR, 52, 253, doi: 10.1016/j.newar.2008.06.006
- Kormendy, J., & Ho, L. C. 2013, ARA&A, 51, 511, doi: 10.1146/annurev-astro-082708-101811
- Koss, M. J., Trakhtenbrot, B., Ricci, C., et al. 2022, ApJS, 261, 6, doi: 10.3847/1538-4365/ac650b

- Kraemer, S. B., Sharma, N., Turner, T. J., George, I. M., & Crenshaw, D. M. 2015, ApJ, 798, 53, doi: 10.1088/0004-637X/798/1/53
- Kraemer, S. B., Turner, T. J., Couto, J. D., et al. 2020, MNRAS, 493, 3893, doi: 10.1093/mnras/staa428
- Król, D. L., Sobolewska, M., Stawarz, L., et al. 2024, ApJ, 966, 201, doi: 10.3847/1538-4357/ad3632
- Ma, J., Elvis, M., Fabbiano, G., et al. 2020, ApJ, 900, 164, doi: 10.3847/1538-4357/abacbe
- —. 2023, ApJ, 948, 61, doi: 10.3847/1538-4357/acba8d
- Maiolino, R., Übler, H., Perna, M., et al. 2024, A&A, 687, A67, doi: 10.1051/0004-6361/202347087
- Marchesi, S., Ajello, M., Comastri, A., et al. 2017, ApJ, 836, 116, doi: 10.3847/1538-4357/836/1/116
- Morganti, R., Tsvetanov, Z. I., Gallimore, J., & Allen,M. G. 1999, A&AS, 137, 457, doi: 10.1051/aas:1999258
- Mukherjee, D., Bicknell, G. V., Sutherland, R., & Wagner,
 A. 2016, MNRAS, 461, 967, doi: 10.1093/mnras/stw1368
 —. 2017, MNRAS, 471, 2790, doi: 10.1093/mnras/stx1749
- Mukherjee, D., Bicknell, G. V., Wagner, A. Y., Sutherland,
 R. S., & Silk, J. 2018, MNRAS, 479, 5544,
 doi: 10.1093/mnras/sty1776
- Nenkova, M., Ivezić, Ž., & Elitzur, M. 2002, ApJL, 570, L9, doi: 10.1086/340857
- Paggi, A., Wang, J., Fabbiano, G., Elvis, M., & Karovska, M. 2012, ApJ, 756, 39, doi: 10.1088/0004-637X/756/1/39
- Ricci, C., Trakhtenbrot, B., Koss, M. J., et al. 2017, ApJS, 233, 17, doi: 10.3847/1538-4365/aa96ad
- Schechter, P. 1976, ApJ, 203, 297, doi: 10.1086/154079
- Schmitt, H. R., Donley, J. L., Antonucci, R. R. J., Hutchings, J. B., & Kinney, A. L. 2003, ApJS, 148, 327, doi: 10.1086/377440
- Siemiginowska, A., Burke, D., Günther, H. M., et al. 2024, ApJS, 274, 43, doi: 10.3847/1538-4365/ad7bab
- Smith, R. K., Brickhouse, N. S., Liedahl, D. A., & Raymond, J. C. 2001, ApJL, 556, L91, doi: 10.1086/322992
- Stawarz, Ł., Ostorero, L., Begelman, M. C., et al. 2008, ApJ, 680, 911, doi: 10.1086/587781
- Travascio, A., Fabbiano, G., Paggi, A., et al. 2021, ApJ, 921, 129, doi: 10.3847/1538-4357/ac18c7
- Trindade Falcao, A., Fabbiano, G., Elvis, M., Paggi, A., & Maksym, W. P. 2023, ApJ, 950, 143, doi: 10.3847/1538-4357/acd052
- Wang, J., Fabbiano, G., Elvis, M., et al. 2011a, ApJ, 736, 62, doi: 10.1088/0004-637X/736/1/62
- Wang, J., Fabbiano, G., Karovska, M., et al. 2009, ApJ, 704, 1195, doi: 10.1088/0004-637X/704/2/1195
- Wang, J., Fabbiano, G., Elvis, M., et al. 2011b, ApJ, 742, 23, doi: 10.1088/0004-637X/742/1/23

Weisskopf, M. C., Brinkman, B., Canizares, C., et al. 2002, PASP, 114, 1, doi: 10.1086/338108

Wilson, A. S., Morse, J. A., Elvis, M., et al. 1996, in Roentgenstrahlung from the Universe, ed. H. U. Zimmermann, J. Trümper, & H. Yorke, 529–530 Wójtowicz, A., Stawarz, ł., Cheung, C. C., et al. 2020, ApJ, 892, 116, doi: 10.3847/1538-4357/ab7930

Yaqoob, T. 2012, MNRAS, 423, 3360, doi: 10.1111/j.1365-2966.2012.21129.x

Zhang, L., García-Bernete, I., Packham, C., et al. 2024a, ApJL, 975, L2, doi: 10.3847/2041-8213/ad81d0

Zhang, L., Packham, C., Hicks, E. K. S., et al. 2024b, ApJ, 974, 195, doi: 10.3847/1538-4357/ad6a4b